Exact domain truncation for the Morse-Ingard equations*

Robert C. Kirby[a,*], Xiaoyu Wei[b], Andreas Klöckner[b]

[a] *Department of Mathematics, Baylor University; Sid Richardson Science Building; 1410 S. 4th St.; Waco, TX 76706; United States*

[b] *Department of Computer Science, University of Illinois at Urbana-Champaign, Champaign, Illinois, United States*

Abstract

Morse and Ingard [1] give a coupled system of time-harmonic equations for the temperature and pressure of an excited gas. These equations form a critical aspect of modeling trace gas sensors. Like other wave propagation problems, the computational problem must be closed with suitable far-field boundary conditions. Working in a scattered-field formulation, we adapt a nonlocal boundary condition proposed in [2] for the Helmholtz equation to this coupled system. This boundary condition uses a Green's formula for the true solution on the boundary, giving rise to a nonlocal perturbation of standard transmission boundary conditions. However, the boundary condition is exact and so Galerkin discretization of the resulting problem converges to the restriction of the exact solution to the computational domain. Numerical results demonstrate that accuracy can be obtained on relatively coarse meshes on small computational domains, and the resulting algebraic systems may be solved by GMRES using the local part of the operator as an effective preconditioner. These numerical results taken together combine several advanced techniques, including higher-order finite elements, geometric multigrid in curvilinear geometry, native use of complex arithmetic, and incorporation of nonlocal operators. These are tied together in a high-level simulation using the Firedrake library.

Keywords: Far field boundary conditions, Finite element, Multiphysics, Thermoacoustics,
MSC[2010] 65N30, 65F08

*This work was supported by NSF SHF-1909176 and SHF-1911019.

*Corresponding author

Email addresses: robert_kirby@baylor.edu (Robert C. Kirby), xywei@illinois.edu (Xiaoyu Wei), andreask@illinois.edu (Andreas Klöckner)

1. Introduction

Laser absorption spectroscopy is used for detecting trace amounts of gases in diverse application areas such as air quality monitoring, disease diagnosis, and manufacturing [3, 4, 5]. In photoacoustic spectroscopy, a laser is focused between the tines of a small quartz tuning fork, and in the presence of a particular gas, acoustic and thermal waves are generated. These waves, in turn, generate mechanical vibration of the tuning fork, and both pyroelectric and piezoelectric effects induce an electric signal that is measured to detect the presence of the gas. Two variants of these sensors are the so-called QEPAS (quartz-enhanced photoacoustic spectroscopy) and ROTADE (resonant optothermoacoustic detection) models [6, 7]. In QEPAS, the acoustic wave dominates the signal, while the thermal wave is more important in ROTADE. While engineered systems typically emphasize one of these waves, a good model should account for both effects.

Earlier work on modeling this problem [8, 9, 10] simplified the model to a single heat or wave equation. Then, an empirical damping term is added to the tuning fork vibration to account for otherwise-neglected processes. This term is generally only available from laboratory experiments with a particular geometry or through analytic calculations in highly-idealized geometry. This approach is only accurate in particular regimes, and the empirical corrections depend strongly on geometry as well as physical parameters. With a more complete model that includes a two-way coupling between the pressure and temperature with the tuning fork deformation, the damping emerges without these specialized empirical corrections. Hence, such a system is far more suitable for design optimization in which the tuning fork geometry is modified to maximize the electric signal.

Accurate simulation of the Morse-Ingard system [1] have been a critical first step in this direction. The Morse-Ingard equations, derived from a linearization of Navier-Stokes, give a coupled heat and wave equation for the temperature and pressure. In the context of trace gas sensing, they include a volumetric forcing term that models the laser heating the trace gas molecules. These equations are posed in a time-harmonic setting, leading to complex-valued Helmholtz-type formulations of the equations. The pressure and temperature on the tuning fork surface are of primary interest, and a fully-coupled model requires carefully chosen boundary conditions to couple these values to the behavior of the tuning fork.

A finite element discretization of the coupled pressure-temperature system was first addressed in [11], where the difficulty of solving the linear system was noted. Kirby and Brennan gave a more rigorous treatment in [12], with analysis of the finite element error and preconditioner performance. Kaderli *et al* derived an analytical solution for the coupled system in idealized geometry in [13]. Their technique involves reformulating the system studied in [12] by an algebraic simplification that eliminates the temperature Laplacian from the pressure equation. In [14], this reformulation was seen to lose coercivity but still retain a Gårding-type inequality, leading to optimal-order finite element convergence theory and preconditioners. Work by Safin *et al* [15] began a more robust multi-physics study, coupling the Morse-Ingard equations for atmospheric pressure and temperature to heat conduction of the quartz tuning fork, although vibrational effects were still not considered. They also applied a perfectly-matched layer (PML) [16] to truncate the computational domain, and a Schwarz-type preconditioner that separates out the PML region was used to effectively reduce the cost of solving the linear system. They also include some favorable comparisons between the computational model and experimental data.

Previous numerical analysis of this problem in the cited literature has focused on volumetric discretizations based on finite elements. In [17], we derived a boundary integral formulation for a scattered-field form of the Morse-Ingard equations. As with other wave problems, this problem writes the solution as the sum of a Morse-Ingard solution that satisfies the forcing (evaluated by means of a fast volumetric convolution with a Green's function) plus a field that satisfies Morse-Ingard with no volumetric forcing but Neumann data on the tuning fork such that the sum satisfies homogeneous boundary conditions. We then formulated a second-kind integral equation for the scattered field and approximated it with a boundary integral method. In this work we return to finite element discretization, but we make use of the results we obtained considering the integral form of the equations to make significant advances in imposing a far-field condition.

In [2], we developed a novel nonlocal boundary condition for truncating the domain of Helmholtz scattering problems. This condition, which uses Green's representation of the solution on the artificial boundary to give a nonlocal Robin-type condition involving layer potentials, is exact – the solution of resulting BVP agrees exactly with the restriction of the solution of the original problem to the computational domain. The resulting finite element stiffness matrix decomposes into "local" and "nonlocal" parts. The local part is exactly that obtained by discretizing the problem subject to transmission boundary conditions. The nonlocal part of the operator includes the layer potentials. It has logical dense subblocks but can be applied in a matrix-free way using fast multipole methods. One preconditions the system matrix by (perhaps approximately) inverting only the local part. We believe that this nonlocal boundary condition offers several potential advantages, both theoretically and computationally, over perfectly matched layers. Because PML solves a perturbed PDE, careful analysis [18] is required to show that the solution to the original PDE is recovered with increasing layer size. However, our method directly discretizes the true PDE and requires no such additional analysis. Second, our method avoids the additional (volume) degrees of freedom in the PML region, leading to smaller linear systems. Finally, multigrid algorithms must be carefully adapted for use with PML For example, the work in [19] uses a custom grid coarsening strategy that doesn't coarsen normal the boundary, limiting the practicality of the method for unstructured meshes, and [20] use special complex-valued and higher-order inter-grid transfers. Without PML, we can precondition the local part of our operator with rather standard multigrid techniques.

Our approach to domain truncation for Helmholtz-type problems builds on other approaches to combine nonlocality or integral operators with finite element discretizations, giving effective boundary truncation without directly perturbing the boundary value problem to be solved. Johnson and Nédélec [21] perform domain truncation by coupling the PDE in the computational domain to a boundary integral equation on the boundary. This approach requires separate unknowns in the volume and for its boundary trace and solutions of the both the volumetric and surface operators. Although not needed for Morse-Ingard, we remark that this method has recently been extended to heterogeneous problems [22]. Keller and Givoli [23] introduce a Dirichlet-to-Neumann or Poincaré-Steklov operator on the boundary, giving a simpler formulation with only a single unknown field. However, using the DtN operator technically requires the solution of an exterior problem with given Dirichlet data, taking the normal derivative of the result. If the boundary of the computational domain has a simple shape, this can be well approximated by a truncated Fourier series. While these methods require (at least approximately) *solving* boundary integral equations, our approach only requires *evaluating* a layer potential a finite distance from the scatterer, hence avoiding any singular integrals or solution processes.

In this paper, we extend the domain truncation in [2] from the Helmholtz operator to the Morse-Ingard system. This extension makes use of several results obtained in [17], where we in fact develop numerical methods based on an integral equation of this system In Section 2, we recall the Morse-Ingard equations. Then, Section 3 addresses far-field boundary conditions for the system and appropriate boundary conditions for domain truncation. By means of the transformation to a decoupled Helmholtz system, we are able to state an analogous far-field condition and associated transmission-type condition for the Morse-Ingard system. This allows a comparison to the *ad hoc* transmission boundary conditions used in [12, 14]. Moreover, we can derive an exact analog of the nonlocal Helmholtz boundary condition for Morse-Ingard.

Although one may directly solve the decoupled Helmholtz equations rather than the coupled form of Morse-Ingard, formulating boundary conditions and directly simulating the coupled system serves several purposes. First, the decoupled formulation leads to lower numerical accuracy than the fully coupled formulation. This reduced accuracy was also observed in integral formulations in [17], and we comment further in Section 6. Second, a more complete model of trace gas sensors [24] involves coupling Morse-Ingard to the tuning fork vibration, which in turn requires modeling the fluid flow. Domain truncation will still be required, but coupling of pressure and temperature to the fluid and tuning fork may limit the utility of the decoupled system. Additionally, as noted in [17], solving for the acoustic mode while neglecting the thermal mode turns out to be an effective approximation. After developing the boundary conditions in Section 3, we derive a finite element formulation for the Morse-Ingard system in Section 4. We discuss the structure of the linear system and approaches to preconditioning in Section 5 and we then provide some numerical in Section 6 before offering some final conclusions in Section 7.

2. The Morse-Ingard equations

The Morse-Ingard equations of thermoacoustics are a system of partial differential equations for the temperature and pressure of an excited gas. The model begins from a time-domain formulation. After assuming time-periodic forcing and performing nondimensionalization and some algebraic manipulations, we arrive at the form given in [13] and further analyzed in [14]:

$$\begin{aligned} -\mathcal{M}\Delta T - iT + i\tfrac{\gamma-1}{\gamma}P &= -S, \\ \gamma\left(1-\tfrac{\Lambda}{\mathcal{M}}\right)T - (1-i\gamma\Lambda)\,\Delta P - \left[\gamma\left(1-\tfrac{\Lambda}{\mathcal{M}}\right)+\tfrac{\Lambda}{\mathcal{M}}\right]P &= i\gamma\tfrac{\Lambda}{\mathcal{M}}S. \end{aligned} \tag{1}$$

Here, T and P are the non-dimensional temperature and pressure, respectively, within the gas. S is a volumetric forcing function, modeling heating of a trace gas by a laser. γ is the ratio of specific heat of the gas at constant pressure to that at constant volume. The dimensionless number $\mathcal{M}$ measures the ratio of the product of the characteristic thermal conduction scale and forcing frequency to sound speed, and Λ does similarly for the viscous length scale. Typical values of parameters would be (to two decimal places)

$$\begin{aligned} \gamma &= 7/5 \\ \mathcal{M} &= 3.66 \cdot 10^{-5} \\ \Lambda &= 5.37 \cdot 10^{-5} \end{aligned} \tag{2}$$

are taken as in [13, 17].

We let $\Omega^c \subset \mathbb{R}^d$ (with $d = 2, 3$) be a bounded domain representing the tuning fork, and let its boundary be called Γ. The complement of $\overline{\Omega^c}$ will be the domain Ω on which we pose (1). On Γ, we impose homogeneous Neumann boundary conditions,

$$\frac{\partial T}{\partial n} = 0, \quad \frac{\partial P}{\partial n} = 0. \tag{3}$$

which posits that the tuning fork is thermally insulated from the gas, and that the tuning fork is sound-hard. More advanced models, in which the gas heats the tuning fork or the acoustic waves couple to tuning fork deformation, generalize this condition [24, 15].

A suitable far-field condition is required to close the model, which requires some appropriate decay at infinity akin to the Sommerfeld radiation condition for the Helmholtz operator. Numerical methods based on volumetric discretization on a truncated domain have posed either some kind of transmission-type condition [12, 14] or perfectly-matched layers [15].

In [17], we gave a boundary integral method for Morse-Ingard based on a scattered-field formulation, which turns the volumetric inhomogeneity into an inhomogeneous Neumann condition on Γ. We discuss this in greater detail in Section 3.2. To arrive at the scattered-field formulation, we split the solution into incoming and scattered waves via

$$T = T^i + T^s, \quad P = P^i + P^s, \tag{4}$$

where T^i and P^i satisfy (1) with the given forcing function S but have some inhomogeneous boundary conditions on Γ. Then, T^s and P^s are chosen to satisfy (1) with homogeneous forcing $S = 0$ and such that the combined waves satisfy (3). The incoming waves T^i and P^i can be constructed by volumetric convolution of S with a free-space Green's function. With these in hand, their normal derivatives on Γ can be computed, and the negative of these used as boundary conditions for T^s and P^s. Consequently, we drop the superscripts 's' for the scattered field and, for the rest of the paper, consider the system of PDE

$$\begin{aligned} -\mathcal{M}\Delta T - iT + i\tfrac{\gamma-1}{\gamma}P = 0, \\ \gamma\left(1-\tfrac{\Lambda}{\mathcal{M}}\right)T - (1-i\gamma\Lambda)\,\Delta P - \left[\gamma\left(1-\tfrac{\Lambda}{\mathcal{M}}\right)+\tfrac{\Lambda}{\mathcal{M}}\right]P = 0, \end{aligned} \tag{5}$$

together with boundary conditions

$$\frac{\partial T}{\partial n} = g_T, \quad \frac{\partial P}{\partial n} = g_P, \tag{6}$$

on Γ together with an appropriate far field condition. Although we obtained satisfactory results with a boundary integral method in [17], we work with volumetric (finite element) discretizations here to chart a path towards modeling of additional volumetric physical phenomena without additional computational machinery in future work. Consequently, in this paper we are primarily interested in developing an analog of the nonlocal boundary condition developed in [2] for the Morse-Ingard system. To this end, we introduce a truncating boundary Σ and define a domain $\Omega' \subset \Omega$ to be that contained between Γ and Σ, as shown in Figure 1.

In [17], we demonstrated that the Morse-Ingard system (1) could be decoupled into a pair of independent Helmholtz equations. After significant algebraic manipulations, we introduce modified material coefficients

$$\begin{aligned} Q^2 &= 4(i\mathcal{M} + \gamma\mathcal{M}\Lambda) + (1 - i\gamma\mathcal{M} - i\Lambda)^2, \\ t_\pm &= \frac{(2\Lambda\gamma - \Lambda - \mathcal{M}\gamma + i)\mathcal{M} \mp i\mathcal{M}Q}{2\gamma(\Lambda - \mathcal{M})(i\Lambda\gamma - 1)} \end{aligned} \tag{7}$$

as well as separate thermal and acoustic wave numbers

$$\begin{aligned} k_t^2 &= \frac{i}{2\mathcal{M}}\left(\frac{1 - i\gamma\mathcal{M} - i\Lambda + Q}{1 - i\gamma\Lambda}\right), \\ k_p^2 &= \frac{i}{2\mathcal{M}}\left(\frac{1 - i\gamma\mathcal{M} - i\Lambda - Q}{1 - i\gamma\Lambda}\right). \end{aligned} \tag{8}$$

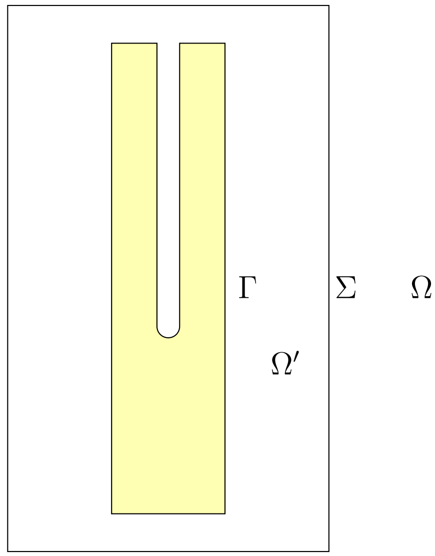

Figure 1: The yellow-shaded area represents the tuning fork. The computational domain Ω is the rectangle minus the tuning fork. Σ is the outer rectangle, and Γ is the boundary of the tuning fork itself.

With the change of variables

$$\begin{bmatrix} V_t \\ V_p \end{bmatrix} = \begin{bmatrix} \mathcal{M} & t_+(1 - i\gamma\Lambda) \\ \mathcal{M} & t_-(1 - i\gamma\Lambda) \end{bmatrix} \begin{bmatrix} T \\ P \end{bmatrix} \equiv B \begin{bmatrix} T \\ P \end{bmatrix}, \tag{9}$$

the Morse-Ingard system (1) decouples into separate Helmholtz equations

$$\begin{aligned} \Delta^2 V_t + k_t^2 V_t &= a_t S, \\ \Delta^2 V_p + k_p^2 V_p &= a_p S, \end{aligned} \tag{10}$$

where a_t and a_p are data-dependent constants. Typical values of these new parameters, again to two decimals, based on those from given above are

$$\begin{aligned} k_t &= 116.81 + 116.82, \\ k_p &= 1 + 3.42 \cdot 10^{-5} i. \end{aligned} \tag{11}$$

For the acoustic mode, k_p has a modest real part and very small imaginary part. Hence, V_p attenuates slowly but can be well-resolved with suitable domain truncation. However, the large real and imaginary parts of k_t suggest that the thermal mode may be difficult to resolve. We also note that the matrix in (9), despite being 2×2 has a condition number on the order of 10^4 and so may amplify roundoff error in practice.

The same change of variables decouples the scattered-field formulation (5). In this case, we have that

$$\begin{aligned} \Delta^2 V_t + k_t^2 V_t &= 0, \\ \Delta^2 V_p + k_p^2 V_p &= 0, \end{aligned} \tag{12}$$

and, by linearity, we take the normal derivative of (9) on Γ to find boundary conditions

$$\begin{bmatrix} \frac{\partial V_T}{\partial n} \\ \frac{\partial V_p}{\partial n} \end{bmatrix} = B \begin{bmatrix} g_T \\ g_P \end{bmatrix} = \begin{bmatrix} \mathcal{M} g_T + t_+(1 - i\gamma\Lambda) g_P \\ \mathcal{M} g_T + t_-(1 - i\gamma\Lambda) g_P \end{bmatrix} \equiv \begin{bmatrix} g_{V_t} \\ g_{V_p} \end{bmatrix}. \tag{13}$$

So, with g_T and g_P given *a priori*, the scattered field formulation of Morse-Ingard can be solved as a pair of decoupled Helmholtz scattering problems.

3. Far field boundary conditions

3.1. Boundary conditions for the Helmholtz problem

We can state far-field boundary conditions for Morse-Ingard and formulate appropriate radiation boundary conditions on Σ by transforming such conditions for each of the decoupled Helmholtz equations in (12). So, we begin with the equation

$$-\Delta u - \kappa^2 u = 0 \tag{14}$$

with $\operatorname{Im} \kappa \geq 0$, posed on Ω, together with Neumann boundary condition

$$\frac{\partial u}{\partial n} = g \tag{15}$$

on the scattering boundary Γ. The relevant boundary condition at infinity is the well-known Sommerfeld radiation condition [25, 26], which requires that

$$\lim_{|x| \to \infty} |x|^{\frac{n-1}{2}} \left(\frac{\partial}{\partial |x|} - i\kappa \right) u = 0. \tag{16}$$

A simple approximate boundary condition arises from imposing Sommerfeld at finite radius, i.e.

$$\left(\frac{\partial}{\partial n} - i\kappa \right) u = 0 \tag{17}$$

on the exterior boundary Σ. This is sometimes called the *transmission* boundary condition. If the exterior boundary Σ is at some radius R away from the origin, this creates an $\mathcal{O}(R^{-2})$ perturbation of u apart from any numerical discretization error, although one may mitigate the computational cost of increasing R by simultaneously increasing the mesh spacing toward the outer boundary [27].

An alternative approach is the technique of *perfectly matched layers* [16, 28], in which one modifies the PDE near the boundary in a so-called *sponge region*. The modified coefficients effectively absorb outgoing waves and allow small computational domains, but the resulting algebraic equations do not yield to efficient techniques such as multigrid. One can use a Schwarz-type method to separately handle the sponge region with a direct solver and the rest of the domain with multigrid or another fast solver [15], although the known method has sub-optimal complexity in three dimensions.

Many *nonlocal* approaches to domain truncation have also been given. Most classically, the Dirichlet-to-Neumann map (DtN) or Stekhlov-Poincaré operator can be used on the artificial boundary. By mapping between types of boundary data, DtN operators require, in principle, the solution of a boundary value problem. In practice, this is often realized by restricting the truncation boundary to (mappings of) a simple geometry in which separation of variables can be performed and then making use of a truncated Fourier series. In [2], we give a new approach to nonlocal boundary conditions that requires only the evaluation of non-singular layer potentials, i.e. a surface convolution with the Helmholtz free-space Green's function or its derivatives. A fast algorithm such as the Fast Multipole Method is useful to avoid quadratic complexity. In its continuous (i.e. not yet discretized) form, this boundary condition is exact, and discretization with any order of accuracy is straightforward. In Subsection 3.3, we recall the formulation of this condition for the Helmholtz operator and develop it for the Morse-Ingard system.

3.2. Far-field conditions for Morse-Ingard

Each of the decoupled Helmholtz equations in (12) must satisfy the Sommerfeld condition, so that

$$\begin{aligned} &\lim_{|x|\to\infty} |x|^{\frac{n-1}{2}} \left(\frac{\partial}{\partial |x|} - ik_t \right) V_t \\ &= \lim_{|x|\to\infty} |x|^{\frac{n-1}{2}} \left(\frac{\partial}{\partial |x|} - ik_p \right) V_p = 0. \end{aligned} \tag{18}$$

In terms of the variables T and P, the Morse-Ingard solution must satisfy

$$\begin{aligned} &\lim_{|x|\to\infty} |x|^{\frac{n-1}{2}} \left(\frac{\partial}{\partial |x|} - ik_t\right) [\mathcal{M}T + t_+(1-i\gamma\Lambda)P] \\ = &\lim_{|x|\to\infty} |x|^{\frac{n-1}{2}} \left(\frac{\partial}{\partial |x|} - ik_p\right) [\mathcal{M}T + t_-(1-i\gamma\Lambda)P] = 0. \end{aligned} \tag{19}$$

Because of the large imaginary part of k_t the thermal mode attenuates very quickly, so some simple boundary condition could be suitable for V_t. The acoustic mode, on the other hand, has only a very small imaginary part and so outgoing waves attenuate very slowly. Since V_p depends on both T and P, however, artificial boundary conditions must act on both of these variables.

We may find an analog to the transmission boundary condition (17) by imposing those conditions on each of the decoupled equations, so that we require

$$\begin{aligned} \left(\frac{\partial}{\partial n} - ik_t\right) V_t = 0, \\ \left(\frac{\partial}{\partial n} - ik_p\right) V_p = 0. \end{aligned} \tag{20}$$

In terms of T and P, we have

$$\begin{aligned} \left(\frac{\partial}{\partial n} - ik_t\right) (\mathcal{M}T + t_+(1-i\gamma\Lambda)P) = 0, \\ \left(\frac{\partial}{\partial n} - ik_p\right) (\mathcal{M}T + t_-(1-i\gamma\Lambda)P) = 0. \end{aligned} \tag{21}$$

With some elementary but involved algebraic manipulation, we have

$$\begin{aligned} \mathcal{M}\frac{\partial T}{\partial n} &= i\left[\frac{t_-k_t - t_+k_p}{t_- - t_+}\right]\mathcal{M}T + i\left[\frac{t_+t_-\left(k_t - k_p\right)}{t_- - t_+}\right](1-i\gamma\Lambda)\,P \\ (1-i\gamma\Lambda)\,\frac{\partial P}{\partial n} &= i\left[\frac{k_p - k_t}{t_- - t_+}\right]\mathcal{M}T + i\left[\frac{t_-k_p - t_+k_t}{t_- - t_+}\right](1-i\gamma\Lambda)\,P \end{aligned} \tag{22}$$

This boundary condition is of course only an approximation of the actually desired far-field condition, in the same sense in which (17) approximates (16), i.e. it becomes exact as Σ moves outward, analogous to the analysis in [27] for Helmholtz.

On the other hand, in prior work [12, 14], we had not yet developed the appropriate Sommerfeld condition for Morse-Ingard and used the *ad hoc* boundary conditions

$$\frac{\partial T}{\partial n} = 0, \quad \frac{\partial P}{\partial n} = i\sqrt{\gamma}P. \tag{23}$$

This condition assumes that no heat is transported from the computational domain and an approximate version of (17) is applied only to the pressure component. Clearly, this boundary condition is quite different from (22). In particular, the outgoing wave for V_p carries both pressure and temperature with it, thus avoiding reliance on the decay of T for accurate imposition of the boundary condition.

Define

$$U = \begin{bmatrix} T \\ P \end{bmatrix}$$

and

$$C = \begin{bmatrix} \mathcal{M} & 0 \\ 0 & 1 - i\gamma\Lambda \end{bmatrix}.$$

Then, boundary conditions (22) and (23) can be written in the form

$$C\frac{\partial U}{\partial n} = iAU, \tag{24}$$

where for (22) we have

$$A = \begin{bmatrix} \frac{t_- k_t - t_+ k_p}{t_- - t_+} & \left(\frac{t_+ t_- (k_t - k_p)}{t_- - t_+}\right)(1 - i\gamma\Lambda) \\ \frac{k_p - k_t}{t_- - t_+} & \left(\frac{t_- k_p - t_+ k_t}{t_- - t_+}\right)(1 - i\gamma\Lambda) \end{bmatrix}, \tag{25}$$

and for (23),

$$A = \begin{bmatrix} 0 & 0 \\ 0 & \sqrt{\gamma}\,(1 - i\gamma\Lambda) \end{bmatrix} \tag{26}$$

Before proceeding, we offer a brief remark on perfectly matched layers for the Morse-Ingard equations. In [15, 29], it was found that PML must be applied to both the temperature and pressure in order to achieve accurate domain truncation. Our discussion of transmission boundary conditions shines further light on this observation. The acoustic mode involves a linear combination of both temperature and pressure, and hence both variables must be damped at the computational boundary in order to avoid spurious reflections.

3.3. Nonlocal boundary conditions

Now, we formulate a nonlocal boundary condition based on a Green's integral representation of the solution. As mentioned, this provides an (in principle) exact boundary condition without the geometric limitations of DtN techniques. We introduced this technique for the Helmholtz operator in [2] and now apply it to Morse-Ingard.

For the Helmholtz problem, we let $\mathcal{K}(x, y)$ be the free-space Green's function, which is given by

$$\mathcal{K}_\kappa(x) := \begin{cases} \frac{i}{4} H_0^{(1)}(\kappa|x|) & d = 2, \\ \frac{i}{4\pi|x|} e^{i\kappa|x|} & d = 3. \end{cases} \tag{27}$$

Here, $H_0^{(1)}$ is the first-kind Hankel function of order 0. We recall Green's representation theorem [25, Thm. 2.5], [30] for the Helmholtz equation:

$$u(x) = D_\kappa(u)(x) - S_\kappa(u)(x) \qquad (x \in \Omega), \tag{28}$$

where D_κ and S_κ refer to the double- and single-layer potentials associated with wave number κ, respectively. These are

$$S_\kappa(u)(x) = \int_\Gamma \mathcal{K}_\kappa(x - y) \tfrac{\partial u}{\partial n_y}(y) dy, \tag{29}$$

$$D_\kappa(u)(x) = \int_\Gamma \left(\tfrac{\partial}{\partial n_y} \mathcal{K}_\kappa(x - y) \right) u(y) dy. \tag{30}$$

Although the double-layer potential is weakly singular, our techniques only require its evaluation away from the singularity on Γ. In anticipation of applying our technique to the decoupled Helmholtz form of Morse-Ingard (10), we include the wave number κ and use distinct layer potentials with $\kappa = k_p, k_t$.

Using the scattering boundary condition (15) on Γ, this becomes (omitting the spatial argument)

$$u = D_\kappa(u) - S_\kappa(g). \tag{31}$$

This representation is valid away from the scattering boundary Γ, and in particular, on Σ. Hence, we can take its normal derivative, so that on Σ

$$\tfrac{\partial u}{\partial n} = \tfrac{\partial}{\partial n} \left(D_\kappa(u) - S_\kappa(g) \right). \tag{32}$$

In [2], we subtracted $i\kappa u$ from each side of (31) and rearranged to arrive at a nonlocal Robin-type boundary condition

$$\tfrac{\partial u}{\partial n} = i\kappa u - \left(i\kappa - \tfrac{\partial}{\partial n}\right)\left(D_\kappa(u) - S_\kappa(g)\right). \tag{33}$$

More generally, we can subtract some $i\sigma$ times u from each side of (31) to write the condition

$$\tfrac{\partial u}{\partial n} = i\sigma u - \left(i\sigma - \tfrac{\partial}{\partial n}\right)\left(D_\kappa(u) - S_\kappa(g)\right), \tag{34}$$

and then (32) is obtained with $\sigma = 0$ and (33) with $\sigma = \kappa$.

Now, we can apply this boundary condition, in either the form (32) or (33) to the decoupled Helmholtz system and back-convert to obtain appropriate nonlocal boundary conditions for Morse-Ingard. As in deriving the local transmission condition, we start with the decoupled form and see what is implied in the coupled form. We let $\boldsymbol{\sigma} = (\sigma_t, \sigma_p)$ be a pair of complex numbers. Then, we apply the boundary condition (34) to each equation of (10) on Σ, so that we have

$$\begin{aligned}\frac{\partial V_t}{\partial n} &= i\sigma_t V_t - \left(i\sigma_t - \frac{\partial}{\partial n}\right)\left(D_{k_t}(V_t) - S_{k_t}(g_{V_t})\right),\\ \frac{\partial V_p}{\partial n} &= i\sigma_p V_p - \left(i\sigma_p - \frac{\partial}{\partial n}\right)\left(D_{k_p}(V_p) - S_{k_p}(g_{V_p})\right).\end{aligned} \tag{35}$$

Now, we substitute in for V_t and V_p via (9), but not in the layer potentials:

$$\begin{aligned}\tfrac{\partial}{\partial n}\left(\mathcal{M}T + t_+(1-i\gamma\Lambda)P\right) =& i\sigma_t\left(\mathcal{M}T + t_+(1-i\gamma\Lambda)P\right) + R_t,\\ \tfrac{\partial}{\partial n}\left(\mathcal{M}T + t_-(1-i\gamma\Lambda)P\right) =& i\sigma_p\left(\mathcal{M}T + t_-(1-i\gamma\Lambda)P\right) + R_p,\end{aligned} \tag{36}$$

where

$$\begin{aligned}R_t &= -\left(i\sigma_t - \tfrac{\partial}{\partial n}\right) D_{k_t}(V_t) + G_t,\\ R_p &= -\left(i\sigma_p - \tfrac{\partial}{\partial n}\right) D_{k_p}(V_p) + G_p,\end{aligned} \tag{37}$$

and $G_t = \left(i\sigma_t - \tfrac{\partial}{\partial n}\right) S_{k_t}(g_{V_t})$ and a similar definition for G_p.

Similar manipulations leading from (21) to (22) let us rearrange these equations to

$$
\begin{aligned}
\mathcal{M}\frac{\partial T}{\partial n} =& i\left[\frac{t_-\sigma_t - t_+\sigma_p}{t_- - t_+}\right]\mathcal{M}T \\
&+ i\left[\frac{t_+t_-\left(\sigma_t - \sigma_p\right)}{t_- - t_+}\right]\left(1 - i\gamma\Lambda\right)P \\
&+ \frac{t_-R_t - t_+R_p}{t_- - t_+}, \\
\left(1 - i\gamma\Lambda\right)\frac{\partial P}{\partial n} =& i\left[\frac{\sigma_p - \sigma_t}{t_- - t_+}\right]\mathcal{M}T \\
&+ i\left[\frac{t_-\sigma_p - t_+\sigma_t}{t_- - t_+}\right]\left(1 - i\gamma\Lambda\right)P \\
&+ \frac{R_p - R_t}{t_- - t_+}.
\end{aligned}
\tag{38}
$$

Note that the nonlocality is contained in R_p and R_t, each of which depend on both T and P through either V_t or V_p.

4. Variational formulation

In this section, we give a finite element formulation of the Morse-Ingard equations (5) under various boundary conditions. First, we establish some notation. We let $L^2(\Omega')$ denote the standard space of complex-valued functions with moduli square-integrable over Ω' and $H^k(\Omega') \subset L^2(\Omega)$ the subspace consisting of functions with weak derivatives up to and including order k also lying in $L^2(\Omega')$. For any Banach space $\mathcal{V}$, we let $\|\cdot\|_{\mathcal{V}}$ denote its norm, with the subscript typically omitted when $\mathcal{V} = L^2(\Omega')$.

The space $L^2(\Omega')$ is equipped with the standard inner product

$$
(f, g) = \int_{\Omega'} f(x)\overline{g(x)}dx, \tag{39}
$$

and we also define the inner product over a portion of the boundary $\tilde{\Gamma} \subset \partial\Omega'$ by

$$
\langle f, g\rangle_{\tilde{\Gamma}} = \int_{\tilde{\Gamma}} f(s)\overline{g(s)}ds. \tag{40}
$$

We partition Ω' into a family of conforming, quasi-uniform triangulations [31] $\{\mathcal{T}_h\}_{h>0}$. Let $\mathcal{V}_h$ be the standard space of continuous piecewise polynomials of some degree $k \geq 1$ over $\mathcal{T}_h$. Since we are dealing with a system of two PDE, we define $\boldsymbol{\mathcal{V}}_h = \mathcal{V}_h \times \mathcal{V}_h$.

We multiply the equations of (5) by the conjugate of the test functions $v, w \in \mathcal{V}_h$, respectively and integrate by parts over Ω'. We let $U = (T, P)$ and $\Psi = (v, w)$. Applying the Neumann boundary conditions (6) on Γ but not taking action yet on Σ, we have

$$\begin{aligned} \mathcal{M}\left(\nabla T, \nabla v\right) - \langle \mathcal{M}\tfrac{\partial T}{\partial n}, v\rangle_\Sigma - i\left(T, v\right) + i\tfrac{\gamma-1}{\gamma}\left(P, v\right) = \langle g_T, v\rangle_\Gamma, \\ \gamma\left(1 - \tfrac{\Lambda}{\mathcal{M}}\right)\left(T, w\right) + \left(1 - i\gamma\Lambda\right)\left[\left(\nabla P, \nabla w\right) - \langle \tfrac{\partial P}{\partial n}, w\rangle_\Sigma\right] \\ - \left[\gamma\left(1 - \tfrac{\Lambda}{\mathcal{M}}\right) + \tfrac{\Lambda}{\mathcal{M}}\right]\left(P, w\right) = \langle g_P, w\rangle_\Gamma. \end{aligned} \tag{41}$$

We add these equations together and define $a_0 : \mathbf{V} \times \mathbf{V} \to \mathbb{C}$ as consisting of the volumetric terms:

$$\begin{aligned} a_0\left(U, \Psi\right) = & \mathcal{M}\left(\nabla T, \nabla v\right) - i\left(T, v\right) + i\tfrac{\gamma-1}{\gamma}\left(P, v\right) \\ & + \gamma\left(1 - \tfrac{\Lambda}{\mathcal{M}}\right)\left(T, w\right) + \left(1 - i\gamma\Lambda\right)\left(\nabla P, \nabla w\right) \\ & - \left[\gamma\left(1 - \tfrac{\Lambda}{\mathcal{M}}\right) + \tfrac{\Lambda}{\mathcal{M}}\right]\left(P, w\right), \end{aligned} \tag{42}$$

and F_0 involving those boundary terms on the right-hand side:

$$F_0(\Psi) = \langle g_T, v\rangle_\Gamma + \langle g_P, w\rangle_\Gamma. \tag{43}$$

Then, we can write (41) as

$$a_0(U, \Psi) - \langle \mathcal{M}\tfrac{\partial T}{\partial n}, v\rangle_\Sigma - (1 - i\gamma\Lambda)\langle \tfrac{\partial P}{\partial n}, w\rangle_\Sigma = F_0(\Psi). \tag{44}$$

At this point, we can close the system by selecting any of the boundary conditions discussed in Section 3 and substituting in the relevant expressions for $\frac{\partial T}{\partial n}$ and $\frac{\partial P}{\partial n}$. Following the general form of the local boundary condition (24), we define a_A by

$$\begin{aligned} a_A(U, \Psi) = & a_0(U, \Psi) - \langle \alpha_{11} T + \alpha_{12} P, v\rangle_\Sigma \\ & - \langle \alpha_{21} T + \alpha_{22} P, w\rangle_\Sigma \end{aligned} \tag{45}$$

with

$$A = \begin{bmatrix} \alpha_{11} & \alpha_{12} \\ \alpha_{21} & \alpha_{22} \end{bmatrix},$$

for the respective A chosen, cf. (25) and (26). This leads to the variational problem of finding $U \in \mathbf{V}$ such that

$$a_A(U, \Psi) = F_0(\Psi) \tag{46}$$

for all $\Psi \in \mathbf{V}$.

We now consider variational problems corresponding to the exact, but nonlocal, boundary conditions. Recall that these boundary conditions are parametrized over the choice of $\boldsymbol{\sigma} = (\sigma_t, \sigma_p)$. Using boundary condition (38) in (41) motivates defining the bilinear form

$$\begin{aligned} a_{\boldsymbol{\sigma}}(U,\Psi) =& a_0(U,\Psi) \\ &+ \langle \tfrac{1}{t_- - t_+} \left[t_- \left(i\sigma_t - \tfrac{\partial}{\partial n}\right) D_{k_t}(V_t) - t_+ \left(i\sigma_p - \tfrac{\partial}{\partial n}\right) D_{k_p}(V_p) \right], v\rangle_\Sigma \\ &+ \langle \tfrac{1}{t_- - t_+} \left(i\sigma_p - \tfrac{\partial}{\partial n}\right) D_{k_p}(V_p) - \tfrac{1}{t_- - t_+} \left(i\sigma_p - \tfrac{\partial}{\partial n}\right) D_{k_t}(V_t), w\rangle_\Sigma \\ \equiv& a_0(U,\Psi) + a^{NL}_{\boldsymbol{\sigma}}(U,\Psi) \end{aligned} \tag{47}$$

and linear form

$$F_{\boldsymbol{\sigma}}(\Psi) = F_0(\Psi) + \langle \tfrac{t_- G_t - t_+ G_p}{t_- - t_+}, v\rangle_\Sigma - \langle \tfrac{G_t - G_p}{t_- - t_+}, w\rangle_\Sigma . \tag{48}$$

Then, we pose the variational problem of finding $U^{\boldsymbol{\sigma}} \in \boldsymbol{\mathcal{V}}$ such that

$$a_{\boldsymbol{\sigma}}(U^{\boldsymbol{\sigma}}, \Psi) = F_{\boldsymbol{\sigma}}(\Psi) \tag{49}$$

for all $\Psi \in \boldsymbol{\mathcal{V}}$. In fact, for any choice of $\boldsymbol{\sigma}$, $U^{\boldsymbol{\sigma}}$ is the solution to (5) with scattering boundary conditions (6) and the Sommerfeld-type far field condition (19).

A standard Galerkin discretization of this problem is obtained by restricting the test function Ψ to $\boldsymbol{\mathcal{V}}_h$, seeking $U^{\boldsymbol{\sigma}}_h \in \boldsymbol{\mathcal{V}}_h$ such that

$$a_{\boldsymbol{\sigma}}(U^{\boldsymbol{\sigma}}_h, \Psi_h) = F_{\boldsymbol{\sigma}}(\Psi_h) \tag{50}$$

for all $\Psi_h \in \boldsymbol{\mathcal{V}}_h$.

Analyzing this discretization follows along the lines proposed in [2] for the scalar Helmholtz problem – one establishes a Gårding inequality for the variational form, by which existing theory [31] for Galerkin methods for elliptic operators provides solvability and optimal H^1 and L^2 and error estimates, subject to a sufficiently fine mesh. We have proven a Gårding-type inequality for the local form of Morse-Ingard in [14], and the same techniques used to handle the nonlocal terms for Helmholtz in [2] can be used for Morse-Ingard. Consequently,

Theorem 4.1. *There exists some $h_0 > 0$ such that for $h \le h_0$, the variational problem* (50) *has a unique solution $U^{\boldsymbol{\sigma}}_h$, and this solution satisfies the best approximation result*

$$\|U^{\boldsymbol{\sigma}} - U^{\boldsymbol{\sigma}}_h\|_{(H^1(\Omega'))^2} \le C \inf_{W_h \in \boldsymbol{\mathcal{V}}_h} \|U^{\boldsymbol{\sigma}} - W_h\|_{(H^1(\Omega'))^2} , \tag{51}$$

and L^2 error estimate

$$\|U^{\boldsymbol{\sigma}} - U_h^{\boldsymbol{\sigma}}\|_{(L^2(\Omega'))^2} \leq Ch \, \|U^{\boldsymbol{\sigma}} - U_h^{\boldsymbol{\sigma}}\|_{(H^1(\Omega'))^2} \,, \tag{52}$$

where the constants C in the two inequalities differ from each other but are independent of h.

5. Linear algebra

A major feature of our nonlocal boundary condition is the opportunity for efficient solvers. For the Helmholtz problem in [2], we demonstrated empirically that preconditioning the entire operator with the local part led to very low GMRES iteration counts. This, of course, means the cost of inverting the local part of the operator drives the overall cost. It is well known that high wave numbers lead to notorious difficulty for iterative methods [32]. Fortunately, this is not the case for the parameter regime of interest for Morse-Ingard. In decoupled form (10), the thermal mode has a large imaginary part to complement the large real part, while the thermal mode has wave number approximately 1. Standard multigrid algorithms handle both of these situations effectively [33], so solving the problem in decoupled form proceeds along lines given in [2], followed by forming T and P from V_t and V_p.

For the fully coupled system, we introduce a basis $\{\psi_i\}_{i=1}^{\dim \boldsymbol{\mathcal{V}}_h}$, and then we can write (50) as a linear system

$$A\mathbf{x} = \mathbf{b}, \tag{53}$$

where

$$\begin{aligned} A_{ij} &= a_{\boldsymbol{\sigma}}(\psi_j, \psi_i), \\ \mathbf{b} &= F_{\boldsymbol{\sigma}}(\psi_j), \end{aligned} \tag{54}$$

and then $U^{\boldsymbol{\sigma}} = \sum_{i=1}^{\dim \boldsymbol{\mathcal{V}}_h} \mathbf{x}_i \psi_i$.

Following the partition of $a_{\boldsymbol{\sigma}}$ given in (47), we can write $A = A^L + A^{NL}$, where

$$\begin{aligned} A_{ij}^L &= a_0(\psi_j, \psi_i), \\ A_{ij}^{NL} &= a_{\boldsymbol{\sigma}}^{NL}(\psi_j, \psi_i), \end{aligned} \tag{55}$$

corresponding to the local and nonlocal parts of the bilinear form.

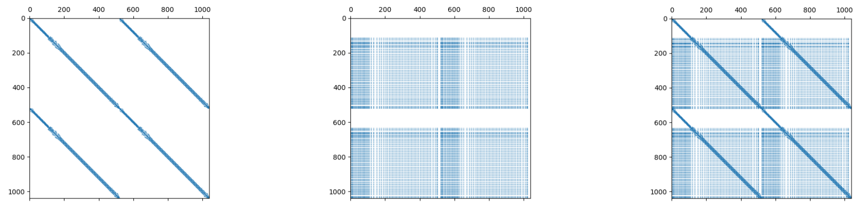

(a) A^L (b) A^{NL} (c) A

Figure 2: Sparsity patterns for the Morse-Ingard stiffness matrix on a coarse mesh with 520 vertices. The contributions from A^L and A^{NL} are shown separately, as well as the combined pattern.

These two matrices have quite different structure. Figure 2 shows their sparsity pattern with piecewise linear basis functions, assuming all degrees of freedom for T are stored contiguously, followed by all degrees of freedom for P. A^L then is a block 2×2 matrix, with each block having the standard sparsity pattern of a P^1 finite element method – entry i, j nonzero when vertices i and j share an edge. This sparsity pattern is shown in Figure 2a. In our implementation, we simply assemble A^L in a standard compressed sparse row format.

On the other hand, A^{NL}_{ij} is nonzero whenever i corresponds to a basis function supported on Σ and j corresponds to a basis function supported on Γ. This leads to logical dense subblocks, which might be expensive to store and operate with. However, the *action* of A^{NL} onto a vector can be evaluated efficiently. As any vector $\mathbf{x}$ of the right size encodes a member $U_{\mathbf{x}} = (T_{\mathbf{x}}, P_{\mathbf{x}})$ of the finite element space, we can write

$$\left(A^{NL}\mathbf{x}\right)_i = \sum_{j=1}^{N} A^{NL}_{ij}\mathbf{x}_j = \sum_{j=1}^{N} a^{NL}_{\boldsymbol{\sigma}}(\psi_j, \psi_i)\mathbf{x}_j = a^{NL}_{\boldsymbol{\sigma}}(U_{\mathrm{x}}, \psi_i). \tag{56}$$

We can efficiently compute this action to high accuracy in three stages. First, we compute the traces of T_{x} and P_{x} on Γ and interpolate them to a quadrature grid obtained using the surface mapping on a quadrature rule from [34] on the reference element. This reduces the layer potential integrals to point potentials. Since source points (on Γ) and target points (on Σ) are well-separated, the kernels are non-singular, allowing the Gaussian-type rules of [34] to provide high accuracy. Then, the point potentials resulting from a^{NL} are evaluated at discrete points on Σ by means of a fast multipole method to interpolate the result into a polynomial space of one degree higher than the finite element space. Finally, these interpolated layer potentials are integrated against basis functions supported on Σ much like load vectors in a standard finite element algorithm.

Solving the linear system with (preconditioned) GMRES [35], a parameter-free algorithm approximating the solution of the in the Krylov subspace by minimizing the equation residual over the Krylov subspace $\text{span}\{A^i\mathbf{b}\}_{i=0}^m$, requires only the action of the matrix-vector product and not the particular matrix entries. Hence, it is suitable for use with the matrix action described above. Unlike conjugate gradients, GMRES is not restricted to operators that are symmetric and positive definite.

For most problems arising in the discretization of PDE, GMRES is most frequently used in conjunction with a *preconditioner*. Mathematically, we multiply the linear system through by some matrix $\widehat{P}^{-1}$:

$$\widehat{P}^{-1}A\mathbf{x} = \widehat{P}^{-1}\mathbf{b}, \tag{57}$$

and so the Krylov space then is $\text{span}\{\left(\widehat{P}^{-1}A\right)^i \widehat{P}^{-1}\mathbf{b}\}_{i=0}^m$.

The overall performance of GMRES typically depends on two factors – the cost of building and applying the operators $\widehat{P}^{-1}$ and A, and the total number of iterations. One hopes to obtain a per-application cost that scales linearly (or log-linearly) with respect to the number of unknowns in the linear system, and a total number of GMRES iterations that is bounded independently of the number of unknowns. We think of $\widehat{P}^{-1}$ being an approximation to the inverse of some matrix P that approximates A. As with the Helmholtz problem in [2], we will take $P = A^L$, the local part of the operator. Unlike A^{NL}, for which only matrix-vector products are available at acceptable cost, we have access to entries of A^L, so applying $\widehat{P}^{-1}$ might correspond to a sparse direct method, an application of some block preconditioner [14], or some other strategy like multigrid.

As a partial justification of our choice of preconditioning matrix, when $\widehat{P} = A^L$ so that the inverse is applied exactly, we arrive at a preconditioned matrix of the form

$$\widehat{P}^{-1}A = \left(A^L\right)^{-1}\left(A^L + A^{NL}\right) = I + \left(A^L\right)^{-1}A^{NL}. \tag{58}$$

Because A^{NL} discretizes a compact operator (layer potential in weak form) and, moreover, $\left(A^L\right)^{-1}$ discretizes the inverse of an elliptic operator, the preconditioned matrix has the form of a (discretization of) a compact perturbation of the identity. We suggested obtaining such a form via preconditioning as a heuristic in [36]. Moret [37] gives rigorous GMRES convergence estimates for this situation once one establishes certain bounds on the operators. In practice, one might replace the inverse of A^L with some approximation, such as a sweep of multigrid. We pursue these options experimentally later in our numerical results section. Blechta [38] has extended Moret's results to describe GMRES convergence for this abstract setting.

6. Numerical results

Now, we present a suite of computational experiments applying our finite element methods and boundary conditions to the Morse-Ingard equations. All of our numerical experiments are conducted using the Firedrake package, a high-level library for the automated solution of partial differential equations [39], leveraging the PETSc library [40, 41] for scalable solutions of the algebraic systems. Firedrake is capable of using higher-order meshes generated with Gmsh [42], so that we can generate (not-quite nested) multigrid hierarchies conforming to the curvilinear tuning fork geometry. At its core, Firedrake provides automation for finite element variational forms described in a domain-specific language called UFL, or 'Unified Form Language' [43]. Our experiments rely on Firedrake's recently-developed 'external operator' capability. This provides a type of 'foreign function interface' from within UFL with two key features. First, it allows users to extend UFL with new operators and have them seamlessly interact with variational forms and their derivatives/adjoints. Second, it allows users to specify evaluation rules, including interfacing to external libraries. These two features allow us to define the boundary conditions involving layer potentials within Firedrake's high-level interface.

Internally, layer potentials are evaluated using our PYTENTIAL package. PYTENTIAL [44] is an open-source, MIT licensed software system for evaluating layer potentials from source geometry represented by unstructured meshes with high accuracy and near-optimal complexity. PYTENTIAL provides for the discretization of a source surface using tools for high-order accurate nonsingular quadrature [34, 45], its refinement according to accuracy requirements [46], and, finally, the evaluation of integral operators via quadrature by expansion (QBX) [47] and the associated GIGAQBX fast algorithm [48], with rigorous accuracy guarantees in two and three dimensions [49]. This fast algorithm, can, in turn make use of FMMLIB [50, 51] for the evaluation of translation operators in the moderate-frequency regime for the Helmholtz operator. In our two-dimensional experiments, we use an FMM order of 15, which provides sufficient accuracy for the accuracy of layer potential evaluation to not limit the overall accuracy obtained. While the integrals in our variational problem do not require the singular integral technology allowed by QBX, it does provide robustness in the case of Σ and Γ are chosen to lie close together.

Our simulations are performed on an Intel Xeon E5-2679 processor on an Ubuntu Linux machine with 256 GB of RAM. Although Firedrake supports distributed-memory parallelism, integration with PYTENTIAL at this level is the subject of future work, with a need to deal with difficulties such as additional required cross-rank data motion. Integrating these approaches to support (and distributed memory) parallelism is the subject of future work.

In all of our experiments, we consider the configuration given in Figure 3. Our experiments do not carry out the conversion to the scattered-field formulation, but start with (5), Neumann boundary conditions (6) on Γ, and various choices of boundary conditions on Σ. The boundary condition on Γ is chosen such that true solution of the system are the pressure and temperature free-space Green's functions associated with a point source given at the red circle in Figure 3. These Green's functions are shown in Figure 4.

Neumann boundary conditions on Σ

Since we are working on problems with analytic solutions, we can pose Neumann boundary conditions on Σ as well as Γ – the normal derivatives of the pressure and temperature in the variational form are replaced by the normal derivatives of the known Green's functions. This allows us to establish a baseline of finite element convergence and compare the accuracy obtained by both coupled and decoupled formulations of Morse-Ingard separately from the discussion of more realistic boundary conditions on Σ. Figure 5a shows the accuracy versus mesh refinement for linear, quadratic, and cubic approximations. Here, we plot the relative error in the $L^2 \times L^2$ graph norm, whose square is given by

$$E^2 = \frac{\|T - T_h\|^2 + \|P - P_h\|^2}{\|T\|^2 + \|P\|^2}.$$

We can also solve the decoupled system (10), with Neumann boundary conditions for V_t and V_p applied on both Γ and Σ, and we should mathematically achieve the same results. However, Figure 5b shows that the numerical

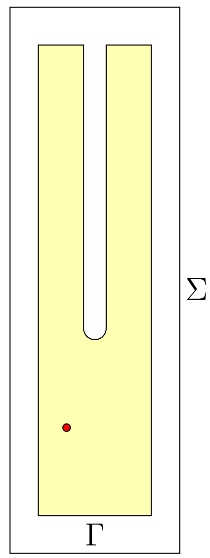

Figure 3: Computational tuning fork domain is the rectangle minus yellow shaded region. Σ is the outer rectangle, and Γ is the boundary of the tuning fork itself. The red circle shows the location of the point source.

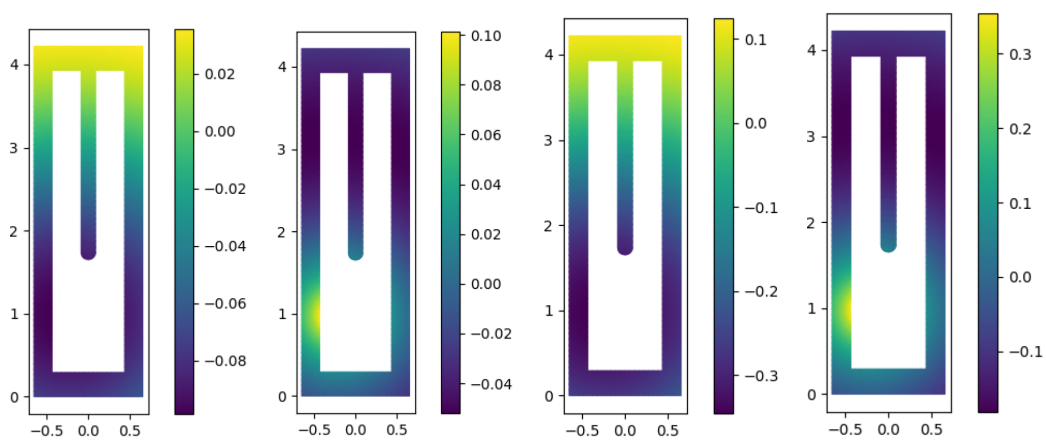

(a) $\mathrm{Re}(G_T)$ (b) $\mathrm{Im}(G_T)$ (c) $\mathrm{Re}(G_P)$ (d) $\mathrm{Im}(G_T)$

Figure 4: Real and imaginary parts of the temperature and pressure Green's functions corresponding to the source shown in Figure 3.

error plateaus at about five digits of relative accuracy. We do not have a fully satisfactory explanation of this, although we note that the transformation (9) between T, P and V_t, V_p has has a condition number on the order of 10^4 (despite being only a 2×2 matrix!). Applying the transformation once to form right-hand side of the decoupled system and then its inverse to produce the physical variables from the computed solution could easily amplify roundoff errors and limit the overall accuracy. The same issue was observed in our boundary integral method for Morse-Ingard in [17] and so seems generic to the decoupled formulation.

We observed in [17] that one can approximate the system in this parameter regime by only solving for the thermal mode V_t, approximating V_p by 0. This requires only solving one Helmholtz equation and produces numerical accuracy comparable to solving the decoupled pair of Helmholtz equations, as shown in Figure 5c.

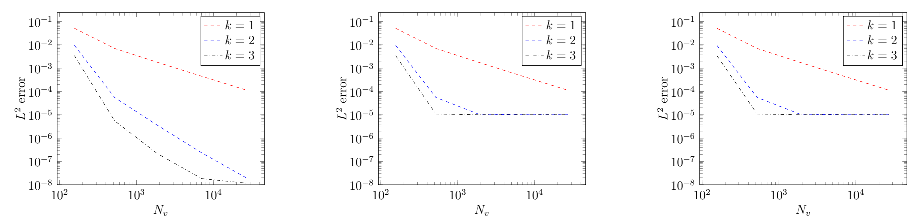

(a) Coupled (b) Decoupled (c) Single equation

Figure 5: Relative $L^2 \times L^2$ accuracy of solving Morse-Ingard equations with Neumann boundary conditions. Coupled, decoupled, and neglecting the thermal mode give comparable solutions on coarse meshes, but the convergence in the decoupled form and single-field forms levels off between 10^{-4} and 10^{-5}.

Transmission boundary conditions on Σ

In practice, we can use Neumann boundary conditions on Γ, but we do not know the Neumann data on Σ. The local transmission boundary conditions (22) and (23) lead to significant perturbations of the boundary value problem and cannot produce the correct answer. Figure 6 demonstrates that we we obtain a relative error of about 0.46 for the “correct” Sommerfeld condition (22) and about 0.51 for the *ad hoc* condition (23). This highlights the need for a more accurate boundary condition on Σ.

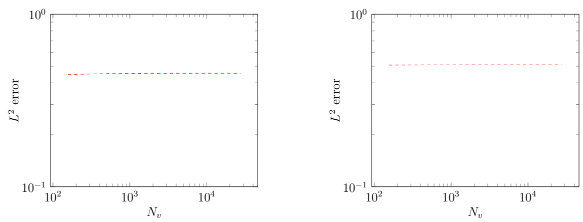

(a) proper (b) *ad hoc*

Figure 6: Relative $L^2 \times L^2$ accuracy of solving Morse-Ingard equations with transmission boundary conditions (22) and (23) with piecewise linear basis functions. Both boundary conditions lead to incorrect answers, and using quadratic or cubic basis functions produce similar results.

Nonlocal boundary conditions on Σ

Next, we consider the nonlocal boundary conditions (38) on Σ. These boundary conditions are exact, and we obtain much greater accuracy than for the local transmission boundary conditions. We do observe a leveling-off of the accuracy under mesh refinement in the fully coupled formulation in Figure 7a, although it obtains more digits of accuracy than the decoupled formulation in Figure 7b or solving only for the acoustic mode V_t and approximating $V_p \approx 0$ in Figure 7c. We do note that (47) requires decoupling transformation to apply the layer potentials to the thermal and acoustic modes, but not a subsequent application to form T and P from the results. Comparing these results, we can conclude that the decoupled form can lead to suitable results if less accuracy is required. In the more general two-way coupled model in [24], boundary conditions coupling the pressure and temperature to the tuning fork work in terms of T and P rather than the decoupled variables. Hence, any advantages gained in solving individual systems would be offset by more complex coupling in the boundary conditions.

Solver performance

Our nonlocal boundary conditions lead to high accuracy without PML, and now we show how multigrid-preconditioned GMRES leads to scalable solution algorithms for the linear system (50). The essential result is that, for our parameters of interest, the linear system is solved in a number of GMRES iterations independent of the mesh parameter and degree of polynomials used in the finite element discretization.

We study two such solution approaches for the coupled formulation of Morse-Ingard with nonlocal boundary conditions. First, at each outer GM-

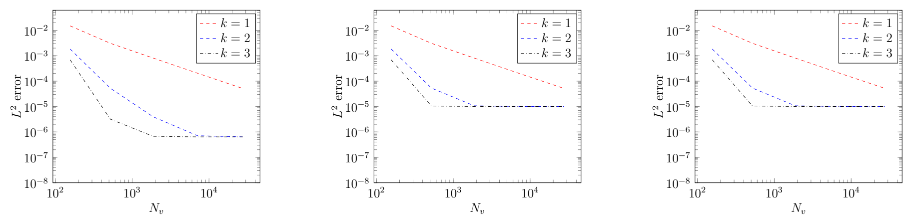

(a) Coupled (b) Decoupled (c) Single equation

Figure 7: Relative $L^2 \times L^2$ accuracy of solving Morse-Ingard equations with the nonlocal boundary condition (38). The coupled form leads to a few more digits of accuracy than the decoupled and single-field formulations.

RES iteration, use the inverse of A^L, itself applied with multigrid-preconditioned GMRES, as a preconditioner. Second, we may just use the multigrid preconditioner for A^L as a preconditioner for the system. This trades the nested iteration needed for inverting A^L for some (hopefully modest) increase in the overall iteration count.

We use a *monolithic* multigrid approach that keeps pressure and temperature coupled together. The smoother is an additive Schwarz decomposition of the finite element spaces into small spaces based on the patch of cells around each vertex in the mesh [52], as shown in Figure 8 for quadratic elements. This smoother requires solving a small, local problems associated with each vertex of the mesh. For symmetric and coercive problems (certainly not Morse-Ingard!) this is known to give condition number estimates independent of the polynomial degree, but in practice seems to perform well for many other problems [53, 54]. These smoothers are readily available in Firedrake through PCPatch [55] and ASMStarPC. On each level of the multigrid hierarchy, we apply two Chebyshev-accelerated iterations of this smoother, solving the coarse grid problem with a sparse LU factorization.

7. Conclusions

We have developed exact truncating boundary conditions for the Morse-Ingard equations. These boundary conditions use a Green's formula representation of the solution in terms of layer potentials and work in general unstructured geometry. The action of the discrete operators may be evaluated efficiently using matrix-free finite elements and a fast multipole method for the layer potentials, and the linear system may be effectively preconditioned with the local part of the operator. Standard convergence theory

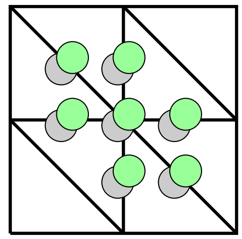

Figure 8: Typical vertex patch smoother for Morse-Ingard discretized with quadratic finite elements. Gray circles indicate pressure unknowns, and green circles indicate temperature unknowns.

holds for the Galerkin discretization, and the method gives good accuracy on small computational domains even with relatively coarse meshes.

In the future, we hope to pursue a rigorous suite of three-dimensional calculations, compute with iterative treatment for A^L, especially as ongoing PYTENTIAL improves its performance for three-dimensional problems. We also hope to study models in which the Morse-Ingard are equations are coupled to the tuning fork displacement.

References

[1] P. M. Morse, K. U. Ingard, Theoretical acoustics, Princeton University Press, Princeton, NJ, 1986.

[2] R. C. Kirby, A. Klöckner, B. Sepanski, Finite elements for Helmholtz equations with a nonlocal boundary condition, SIAM Journal on Scientific Computing 43 (3) (2021) A1671–A1691.

[3] R. F. Curl, F. Capasso, C. Gmachl, A. A. Kosterev, B. McManus, R. Lewicki, M. Pusharsky, G. Wysocki, F. K. Tittel, Quantum cascade lasers in chemical physics, Chemical Physics Letters 487 (1-3) (2010) 1–18.

[4] P. Patimisco, G. Scamarcio, F. K. Tittel, V. Spagnolo, Quartz-enhanced photoacoustic spectroscopy: a review, Sensors 14 (4) (2014) 6165–6206.

[5] J. C. Petersen, L. Lamard, Y. Feng, J.-F. Focant, A. Peremans, M. Lassen, Quartz-enhanced photo-acoustic spectroscopy for breath analyses, in: Optics and Biophotonics in Low-Resource Settings III, Vol. 10055, International Society for Optics and Photonics, 2017, p. 1005503.

[6] A. A. Kosterev, Y. A. Bakhirkin, R. F. Curl, F. K. Tittel, Quartz-enhanced photoacoustic spectroscopy, Optics Letters 27 (21) (2002) 1902–1904.

[7] A. A. Kosterev, J. H. D. III, Resonant optothermoacoustic detection: Technique for measuring weak optical absorption by gases and micro-objects, Optics Letters 35 (21) (2010) 3571–3573.

[8] N. Petra, Mathematical modeling, analysis, and simulation of trace gas sensors, Ph.D. thesis, University of Maryland (2010).

[9] N. Petra, J. Zweck, A. A. Kosterev, S. E. Minkoff, D. M. Thomazy, Theoretical analysis of a quartz-enhanced photoacoustic spectroscopy sensor, Applied Physics B: Lasers and Optics 94 (4) (2009) 673–680.

[10] N. Petra, J. Zweck, S. E. Minkoff, A. A. Kosterev, J. H. D. III, Modeling and design optimization of a resonant optothermoacoutstic trace gas sensor, SIAM J Appl Math 71 (2001) 309–332.

[11] B. Brennan, R. C. Kirby, J. Zweck, S. Minkoff, High-performance Python-based simulations of trace gas sensors, Proceedings of PyHPC workshop (2013).

[12] B. Brennan, R. C. Kirby, Finite element approximation and preconditioners for a coupled thermal–acoustic model, Computers & Mathematics with Applications 70 (10) (2015) 2342–2354.

[13] J. Kaderli, J. Zweck, A. Safin, S. E. Minkoff, An analytic solution to the coupled pressure–temperature equations for modeling of photoacoustic trace gas sensors, Journal of Engineering Mathematics 103 (1) (2017) 173–193.

[14] R. C. Kirby, P. Coogan, Optimal-order preconditioners for the Morse–Ingard equations, Computers & Mathematics with Applications 79 (8) (2020) 2458–2471.

[15] A. Safin, S. Minkoff, J. Zweck, A preconditioned finite element solution of the coupled pressure-temperature equations used to model trace gas sensors, SIAM Journal on Scientific Computing 40 (5) (2018) B1470–B1493.

[16] J.-P. Berenger, A perfectly matched layer for the absorption of electromagnetic waves, Journal of Computational Physics 114 (2) (1994) 185–200.

[17] X. Wei, A. Klöckner, R. C. Kirby, Integral equation methods for the Morse-Ingard equations, Journal of Computational Physics 112416 (2023).

[18] M. Lassas, E. Somersalo, On the existence and convergence of the solution of PML equations, Computing 60 (3) (1998) 229–241.

[19] C. C. Stolk, M. Ahmed, S. K. Bhowmik, A multigrid method for the Helmholtz equation with optimized coarse grid corrections, SIAM Journal on Scientific Computing 36 (6) (2014) A2819–A2841.

[20] V. Dwarka, C. Vuik, Stand-alone multigrid for helmholtz revisited: Towards convergence using standard components, arXiv preprint arXiv:2308.13476 (2023).

[21] C. Johnson, J.-C. Nédélec, On the coupling of boundary integral and finite element methods, Mathematics of Computation (1980) 1063–1079.

[22] E. P. Stephan, T. Tran, FEM–BEM coupling, Schwarz Methods and Multilevel Preconditioners for Boundary Element Methods (2021) 331–366.

[23] J. B. Keller, D. Givoli, Exact non-reflecting boundary conditions, Journal of computational physics 82 (1) (1989) 172–192.

[24] A. Mozumder, A. Safin, S. E. Minkoff, J. Zweck, A two-way coupled model of visco-thermo-acoustic effects in photoacoustic trace gas sensors, SIAM Journal on Applied Mathematics 83 (3) (2023) 1074–1097.

[25] D. Colton, R. Kress, Inverse Acoustic and Electromagnetic Scattering Theory, 2nd Edition, Springer, 1998.

[26] A. Sommerfeld, Die Greensche funktion der schwingungsgleichung, J. Ber. Deutsch Math. Verein 21 (1912) 309–353.

[27] C. I. Goldstein, The finite element method with non-uniform mesh sizes applied to the exterior Helmholtz problem, Numerische Mathematik 38 (1) (1982) 61–82.

[28] V. Druskin, S. Güttel, L. Knizhnerman, Near-optimal perfectly matched layers for indefinite Helmholtz problems, SIAM Review 58 (1) (2016) 90–116. doi:10.1137/140966927.
URL https://doi.org/10.1137/140966927

[29] A. K. Safin, Modeling trace gas sensors with the coupled pressure-temperature equations, Ph.D. thesis, The University of Texas at Dallas (2018).

[30] C. H. Wilcox, A Generalization of Theorems of Rellich and Atkinson, Proceedings of the American Mathematical Society 7 (2) (1956) 271–276. doi:10.2307/2033184.
URL https://www.jstor.org/stable/2033184

[31] S. Brenner, L. Scott, The Mathematical Theory of Finite Element Methods, Springer, New York, NY, 2007.

[32] O. G. Ernst, M. J. Gander, Why it is difficult to solve Helmholtz problems with classical iterative methods, in: Numerical analysis of multiscale problems, Springer, 2012, pp. 325–363.

[33] M. J. Gander, I. G. Graham, E. A. Spence, Applying GMRES to the Helmholtz equation with shifted laplacian preconditioning: what is the largest shift for which wavenumber-independent convergence is guaranteed?, Numerische Mathematik (2015) 1–48.

[34] H. Xiao, Z. Gimbutas, A numerical algorithm for the construction of efficient quadrature rules in two and higher dimensions, Computers & Mathematics with Applications 59 (2) (2010) 663–676. doi:10.1016/j.camwa.2009.10.027.

[35] Y. Saad, M. H. Schultz, GMRES: A generalized minimal residual algorithm for solving nonsymmetric linear systems, SIAM Journal on scientific and statistical computing 7 (3) (1986) 856–869.

[36] V. E. Howle, R. C. Kirby, Block preconditioners for finite element discretization of incompressible flow with thermal convection, Numerical Linear Algebra with Applications 19 (2) (2012) 427–440.

[37] I. Moret, A note on the superlinear convergence of GMRES, SIAM journal on numerical analysis 34 (2) (1997) 513–516.

[38] J. Blechta, Stability of linear GMRES convergence with respect to compact perturbations, SIAM Journal on Matrix Analysis and Applications 42 (1) (2021) 436–447.

[39] F. Rathgeber, D. A. Ham, L. Mitchell, M. Lange, F. Luporini, A. T. T. McRae, G.-T. Bercea, G. R. Markall, P. H. J. Kelly, Firedrake: automating the finite element method by composing abstractions, ACM Transactions on Mathematical Software 43 (3) (2016) 24:1–24:27. `arXiv:1501.01809`, `doi:10.1145/2998441`.

[40] S. Balay, S. Abhyankar, M. F. Adams, S. Benson, J. Brown, P. Brune, K. Buschelman, E. Constantinescu, L. Dalcin, A. Dener, V. Eijkhout, J. Faibussowitsch, W. D. Gropp, V. Hapla, T. Isaac, P. Jolivet, D. Karpeev, D. Kaushik, M. G. Knepley, F. Kong, S. Kruger, D. A. May, L. C. McInnes, R. T. Mills, L. Mitchell, T. Munson, J. E. Roman, K. Rupp, P. Sanan, J. Sarich, B. F. Smith, S. Zampini, H. Zhang, H. Zhang, J. Zhang, PETSc/TAO users manual, Tech. Rep. ANL-21/39 - Revision 3.20, Argonne National Laboratory (2023). `doi:10.2172/1968587`.

[41] S. Balay, W. D. Gropp, L. C. McInnes, B. F. Smith, Efficient management of parallelism in object oriented numerical software libraries, in: E. Arge, A. M. Bruaset, H. P. Langtangen (Eds.), Modern Software Tools in Scientific Computing, Birkhäuser Press, 1997, pp. 163–202.

[42] C. Geuzaine, J.-F. Remacle, Gmsh: A 3-D finite element mesh generator with built-in pre-and post-processing facilities, International journal for numerical methods in engineering 79 (11) (2009) 1309–1331.

[43] M. S. Alnæs, A. Logg, K. B. Ølgaard, M. E. Rognes, G. N. Wells, Unified Form Language: A domain-specific language for weak formulations of partial differential equations, ACM Transactions on Mathematical Software 40 (2) (2014) 9:1–9:37. `arXiv:1211.4047`, `doi:10.1145/2566630`.

[44] A. Klöckner, et al., pytential Source Code Repository (2020).
URL `https://github.com/inducer/pytential`

[45] A. Klöckner, et al., meshmode Source Code Repository (2020).
URL `https://github.com/inducer/meshmode`

[46] M. Wala, A. Klöckner, A fast algorithm for Quadrature by Expansion in three dimensions, Journal of Computational Physics 388 (2019) 655–689. doi:10.1016/j.jcp.2019.03.024.
URL http://www.sciencedirect.com/science/article/pii/S0021999119302074

[47] A. Klöckner, A. Barnett, L. Greengard, M. O'Neil, Quadrature by expansion: A new method for the evaluation of layer potentials, Journal of Computational Physics 252 (2013) 332 – 349. doi:10.1016/j.jcp.2013.06.027.

[48] M. Wala, A. Klöckner, A fast algorithm with error bounds for Quadrature by Expansion, Journal of Computational Physics 374 (2018) 135–162. doi:10.1016/j.jcp.2018.05.006.
URL http://www.sciencedirect.com/science/article/pii/S0021999118302985

[49] M. Wala, A. Klöckner, On the Approximation of Local Expansions of Laplace Potentials by the Fast Multipole Method, arXiv:2008.00653 [cs, math]ArXiv: 2008.00653 (Aug. 2020).
URL http://arxiv.org/abs/2008.00653

[50] Z. Gimbutas, L. Greengard, A fast and stable method for rotating spherical harmonic expansions, Journal of Computational Physics 228 (16) (2009) 5621–5627. doi:10.1016/j.jcp.2009.05.014.
URL http://www.sciencedirect.com/science/article/pii/S0021999109002691

[51] A. Klöckner, et al., pyfmmlib Source Code Repository (2020).
URL https://github.com/inducer/pyfmmlib

[52] J. Schöberl, J. M. Melenk, C. Pechstein, S. Zaglmayr, Additive Schwarz preconditioning for p-version triangular and tetrahedral finite elements, IMA Journal of Numerical Analysis 28 (2008) 1–24. doi:10.1093/imanum/drl046.

[53] R. Abu-Labdeh, S. MacLachlan, P. E. Farrell, Monolithic multigrid for implicit Runge-Kutta discretizations of in compressible fluid flow, Journal of Computational Physics 478 (2023) 111961.
URL https://doi.org/10.1016/j.jcp.2023.111961

[54] V. John, G. Matthies, Higher-order finite element discretizations in a benchmark problem for incompressible flows, International Journal for Numerical Methods in Fluids 37 (8) (2001) 885–903.

[55] P. E. Farrell, M. G. Knepley, L. Mitchell, F. Wechsung, PCPATCH: software for the topological construction of multigrid relaxation methods, ACM Transactions on Mathematical Software (TOMS) 47 (3) (2021) 1–22.